MATLAB®-Based Flight-Dynamics and Flutter Modeling of a Flexible Flying-Wing Research Drone

Dr. David K. Schmidt[*]
University of Colorado[†]
dschmidt@uccs.edu

Abstract

A relatively low-order, linear dynamic model is developed for the longitudinal flight-dynamics analysis of a flexible, flying-wing research drone, and results are compared to previously published results. The model includes the dynamics of both the rigid-body and elastic degrees of freedom, and the subject vehicle is designed to flutter within its flight envelope. The vehicle of interest is a 12-pound unmanned, flying-wing aircraft with a wingspan of 10 ft. In the modeling, the rigid-body degrees of freedom (DOFs) are defined in terms of motion of a vehicle-fixed coordinate frame, as required for flight-dynamics analysis. As a result, the state variables corresponding to the rigid-body DOFs are identical to those used in modeling a rigid vehicle, and the additional states are associated with the elastic degrees of freedom. Both body-freedom and bending-torsion flutter conditions are indicated by the model, and it is shown that the flutter speeds, frequencies, and genesis modes suggested by this low-order model agree very well with the analytical predictions and flight-test results reported in the literature. The longitudinal dynamics of the vehicle are characterized by a slightly unstable phugoid mode, a well-damped, pitch-dominated, elastic-short-period mode, and the stable or unstable aeroelastic modes. A classical, rigid-body, short-period mode does not exist.

1. Introduction

We seek to develop a linear dynamic model for the dynamic analysis of a flexible, flying-wing research drone. This model must capture the dynamics of both the rigid-body and elastic degrees of freedom. Such models, sometimes called n-degrees-of-freedom, or NDOF models, are especially important here because the vehicle under study was designed to flutter within its flight envelope. Therefore, the dynamic models to be developed must appropriately capture key aspects of the vehicles dynamics, including the critical flutter conditions.

We will utilize a modeling methodology that can yield relatively simple dynamic models that provide insight into the vehicle's dynamics, and can be available early in the design-cycle, as opposed to later, which is frequently the case for NDOF models. We also require that our models can be easily updated, as more accurate data become available. Typically NDOF models are not available until quite late in the cycle, due in part to the level of detail used in developing

---

[*] Fellow, AIAA
[†] Professor Emeritus

the models. Detailed finite-element models (FEMs) require the detailed structural design to be available. And of course such information only becomes available late in the design. Plus, such detailed models lead to high dynamic order. For example, in the NDOF modeling work reported in Ref. 1 the NASTRAN FEM contained 2556 degrees of freedom (DOFs), while the doublet-lattice unsteady-aerodynamic model had 2252 aerodynamic DOFs. Finally, strictly numerical models are sometimes less transparent than analytic or semi-analytic models, in terms of developing insight into the system.

We will utilize a modeling approach that fundamentally differs from that frequently taken in developing NDOF models (c.f., Refs. 2-3). Sophisticated modeling techniques have been developed within the aeroelasticity/structural-dynamics communities for flutter and loads predictions in aircraft design, and these tools and methodologies have been tailored and optimized to accomplish these specific objectives. Traditionally, these models only considered the elastic DOFs. With coupling between the rigid-body and elastic degrees of freedom now becoming more prevalent, these traditional flutter-analysis tools are being extended in an attempt to also capture the rigid-body DOFs. In contrast, one may view our approach as beginning with a rigid-body flight-dynamics model and extending it to include the elastic degrees of freedom.

Major differences exist between flutter-modeling approaches and models developed for flight-dynamics analysis. These differences typically involve including or excluding rigid body DOFs, for example flutter models typically exclude the surge-translation rigid-body degree of freedom, hence eliminating the phugoid mode. But the primary differences between the two modeling approaches involve the coordinate frames used in deriving the equations of motion, and the model format. In flutter models all the DOFs, as well as aerodynamic forces and moments, are defined in inertial coordinates, or in an inertial reference frame, while in flight-dynamics modeling the rigid-body DOFs, forces, and moments are always defined in vehicle-fixed, non-inertial coordinates. The latter approach yields time-invariant vehicle-mass properties (for strictly rigid vehicles) and is compatible with typical on-board sensor measurements. The use of inertial coordinates in the flutter models thus requires extensive modifications and transformations of the results to allow for the merger of these results with the flight-dynamics model governing the rigid-body degrees of freedom (Refs. 2 and 3). We avoid such transformations by working entirely in the vehicle-fixed, non-inertial reference frame.

The model formats also differ drastically between the flutter models and flight-dynamics models. The former are almost always numerical models or computer codes, while the latter is frequently a semi-analytical model, in which parameters (e.g., aerodynamic stability derivatives) may be updated easily as they become available. Furthermore, useful state-variable definitions in the flight-dynamics models help yield insight into the results. As will be noted in Section 6, the states corresponding to the rigid-body degrees of freedom in the flight-dynamics model presented in this paper are identical to those in a rigid-body flight-dynamics model.

The modeling approach to be utilized, depicted in Fig. 1 and taken from Refs. 4 and 5, is consistent with conventional aeroelastic theory (c.f., Ref. 6), but develops an integrated NDOF model from first principles using a vehicle-fixed, or non-inertial, reference frame from the outset. Plus, as will be seen later, the state definitions in this NDOF model are more consistent with conventional flight-dynamic models, thus making the dynamics more transparent and the model results easier to interpret and validate. The dashed box in Fig. 1 indicates that unsteady aerodynamics may or may not be specifically included in the modeling. Finally, to meet the second goal of obtaining dynamic models earlier in the design cycle, a simpler FEM model, implemented in a MATLAB® script, is used to obtain the vibration solution, a variety of methods

are used to estimate the rigid-body stability derivatives, and quasi-steady or unsteady strip-theoretic techniques (Refs. 4-7), also implemented in a MATLAB[®] script, are applied to estimate the aeroelastic stability derivatives (or aerodynamic influence coefficients).
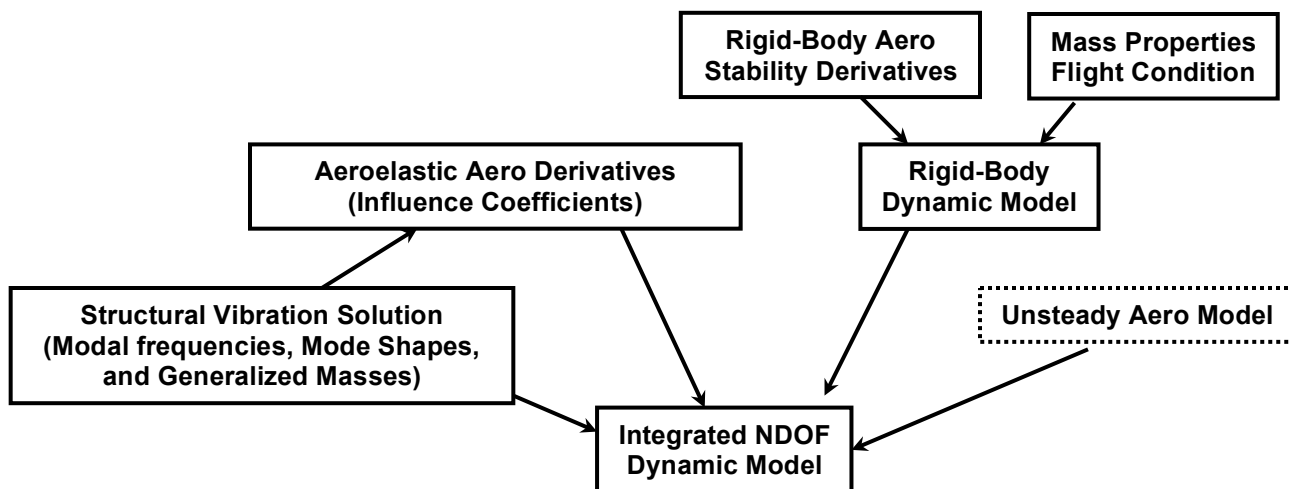

Figure 1, Modeling Methodology

2. Vehicle Description

The vehicle of interest, depicted in Figs. 2 and 3, is Lockheed Martin's Body-Freedom-Flutter (BFF) vehicle, a 12-pound unmanned, flying-wing research aircraft with a 10 ft wingspan (Refs. 17,18). One of these vehicles (BFF06) was provided[‡] for flight research to the Unmanned Air Vehicle (UAV) Lab of the University of Minnesota (UMN), and the author is collaborating with UMN on this research. These vehicles are precursors to the unmanned, multi-utility X-56A vehicle currently undergoing flight testing at NASA's Armstrong Flight Research Center. The BFF vehicle was designed to exhibit two symmetric flutter conditions in the longitudinal dynamics, involving the first two or three symmetric vibration modes. Traditional bending-torsion aeroelastic flutter is also exhibited in the lateral-directional dynamics, but the focus here will be on the longitudinal dynamics.

The BFF is a low-speed swept-back flying wing with winglets on the wing tips for directional stability and an electric motor driving a pusher propeller (not shown in the figure) mounted at the top rear of the rigid center body. The entire trailing edge of the wing consists of eight control surfaces. The
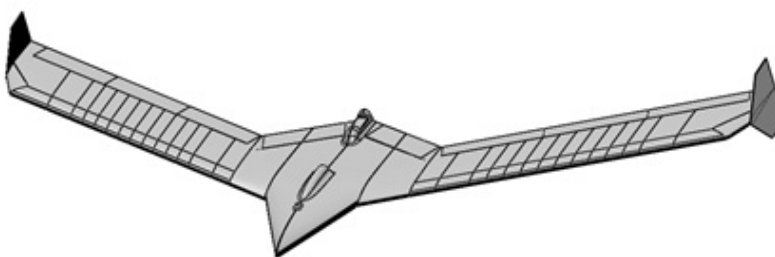
Figure 2, Vehicle Configuration

---

‡ This transfer was facilitated by Mr. Peter Flick of the AFRL.

vehicle's mass properties, provided by the UMN (Ref. 8), and the planform characteristics are summarized in Tables A1 and A2 in Section 11, Appendix A. Note that this is a fairly small, lightweight, unmanned vehicle.
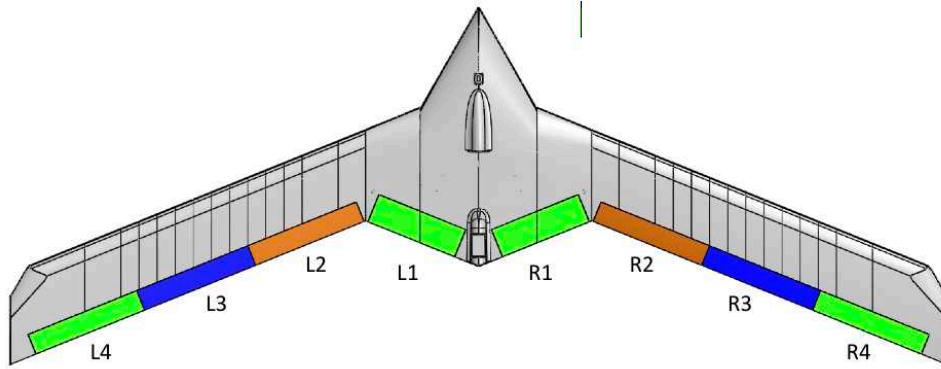
Figure 3, Vehicle Planform

3. Rigid-Body Longitudinal Dynamics

The rigid-body aerodynamic characteristics of the vehicle were estimated using classical/semi-empirical methods as presented in the USAF Stability and Control DATCOM (Ref. 9). This analysis was performed using the legacy FORTRAN code Digital DATCOM (Ref. 10), executed on a 64-bit Mac Pro desktop computer using a public-domain FORTRAN compiler. All other numerical analyses were performed in MATLAB®. Future flight tests are planned by the UMN, and as that test data become available the rigid-body aerodynamic data may be easily updated.

The estimated rigid-body stability derivatives are presented in Table B1 in Section 11, Appendix B. Based on these data note that the rigid vehicle is statically stable, with a static margin of

$$ SM = \frac{-C_{M_\alpha}}{C_{L_\alpha}} = \frac{0.310}{4.074} = 7.6\% $$

Also note that the $\dot{\alpha}$ derivatives, primarily associated with lag of downwash on a trailing lifting surface, are typically negligible on a flying wing. No direct comparison between these data and Lockheed Martin's was performed, since rigid-body aerodynamics were not reported in Ref. 1.

For a flight condition corresponding to level flight at 1000 ft altitude and a velocity of 60 fps, the transfer functions for the pitch-attitude and plunge-acceleration (at the *cg*) responses from symmetric deflections of surfaces L3 and R3 shown in Fig. 3 (defined here as elevator deflections δ_E) are

$$ \frac{\theta_{cg}(s)}{-\delta_E(s)} = \frac{105\ [0.049][6.66]}{[-0.01, 0.54][0.73, 12.43]} \quad \text{deg/deg} $$

1

$$ \frac{n_{Z-cg}(s)}{-\delta_E(s)} = \frac{109\ [0][-0.285][0.3617][5.64]}{[-0.01, 0.54][0.73, 12.43]} \quad \text{ft/sec}^2/\text{deg} $$

(Here a shorthand notation in used. Two terms in square brackets denote the damping and frequency of a quadratic polynomial, and a single term in brackets denotes the negative of the root of a first-order polynomial.) The phugoid mode is slightly unstable with a natural frequency of 0.54 rad/sec, while the short period is stable and well damped with a natural frequency of 12.4 rad/sec. Also, the attitude numerator roots are $1/T_{\theta_1} = 0.049$ /sec and $1/T_{\theta_2} = 6.66$ /sec.

The eigenvector, or mode shape, for the short-period mode is depicted in Fig. 4, and a traditional short-period mode shape is evident (See Ref. 4 Chapter 10.). That is, the mode is dominated by the pitch-rate response, with angle of attack and pitch attitude making moderate contributions to the modal response. These latter two responses, furthermore, lag the pitch rate by a little over 90 deg in phase. The contribution of surge velocity u to the short-period response is so small it cannot be plotted in the figure. All these characteristics are indicative of a traditional short-period mode. The other eigenvector associated with the phugoid mode is dominated by surge velocity, again as typical. Note that rather conventional aircraft attitude dynamics are exhibited.

θ, rad α, rad q, rad/sec
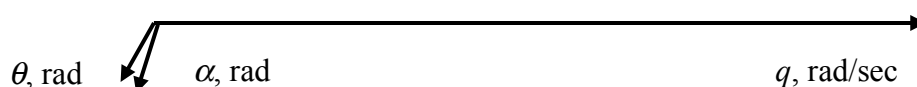
**Figure 4, Short-Period Eigenvector (Mode Shape)**

As the flight velocity increases from near 60 fps to approximately 100 fps, the longitudinal modal eigenvalues migrate as shown in Fig. 5. The short-period mode remains stable and well damped, while the locations of the phugoid poles change little.
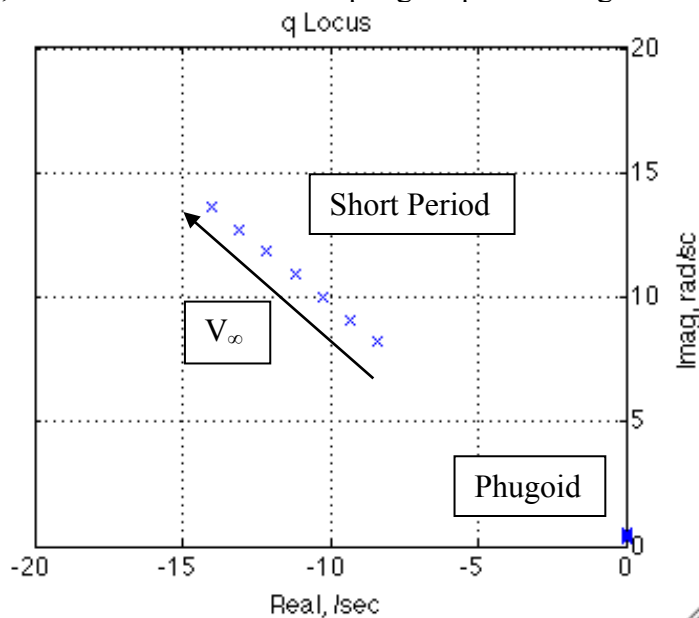
Figure 5, Longitudinal Dynamic-Pressure Root Locus (Rigid Vehicle)

4. Structural Vibration Characteristics

As noted in Section 1, a relatively simple FEM developed in MATLAB® at the UMN (Ref. 11) was used to characterize the vehicle's structural-vibration properties. Simple beam elements and only 14 nodes were used, resulting in 42 structural DOFs in this model. The nodal geometry and structural coordinate frame used in the FEM are shown in Fig. 6. This FEM, along with ground-vibration tests (GVT) performed at the UMN (Ref. 12), were used to obtain the free-vibration modal frequencies and damping ratios, mode shapes, and generalized masses used in our model development.
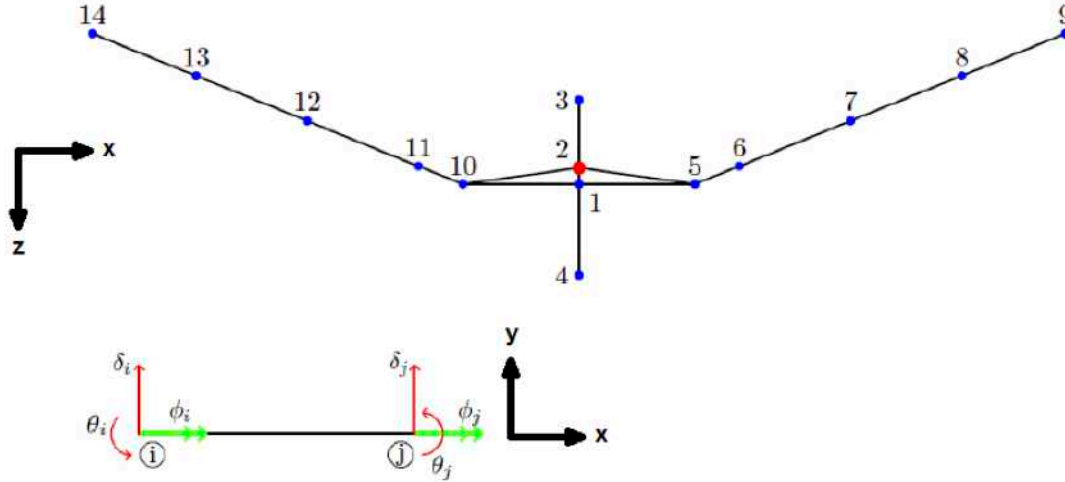
Figure 6, Finite-Element Coordinate Frame and Node Schematic

The vibration-modal results are summarized in Table 1 for the first three of the seven symmetric modes from the FEM, along with some results from Ref. 1. There is good agreement in modal frequency for the first bending mode, but the FEM analysis predicted the frequency of the second and third modes to be significantly lower and higher, respectively, than those obtained in the GVTs, as well as those listed in Ref. 1. These frequency differences are still under investigation, but in our modeling effort reported here the GVT frequencies of 117.8 rad/sec and 145.6 rad/sec will be used for the second and third modes, along with the other modal frequency and damping ratios obtained from the UMN GVTs. Modal damping ratios and generalized masses were not reported in Ref. 1, so no comparisons could be made among these parameters.

Table 1, Structural Vibration Characteristics

Data and Source	Sym 1st Bending	Sym 1st Torsion	Sym 2nd Bending
Frequency, UMN FEM	34.9 r/s	94.5 r/s	163.2 r/s
Frequency, UMN GVT	34.6 r/s	117.8 r/s	145.6 r/s
Frequency, LM (Ref. 1)	35.4 r/s	123.4 r/s	147.3 r/s
Damping, UMN GVT	1.55%	2.06%	2.85%
Gen. Mass, UMN FEM	0.28950 sl-ft^2	0. 00772 sl-ft^2	0. 05239 sl-ft^2

The mode shapes for these first three symmetric modes obtained from the UMN FEM are shown in Figs. 7-9, respectively. These mode shapes agree qualitatively with those presented in Ref. 1. The plunge-translational displacement (Z vehicle positive down) and wing torsional (pitch θ positive leading-edge up) displacement along the wing elastic axis are both indicated. Consequently, it is clear from Fig. 7, for example, that the first symmetric mode exhibits simultaneous (tips-down) bending and (leading-edge-down) torsional displacements, but is referred to herein as a "bending" mode. The second symmetric mode shape in Fig. 8 exhibits almost pure torsional displacement. Chord-wise bending is not considered.
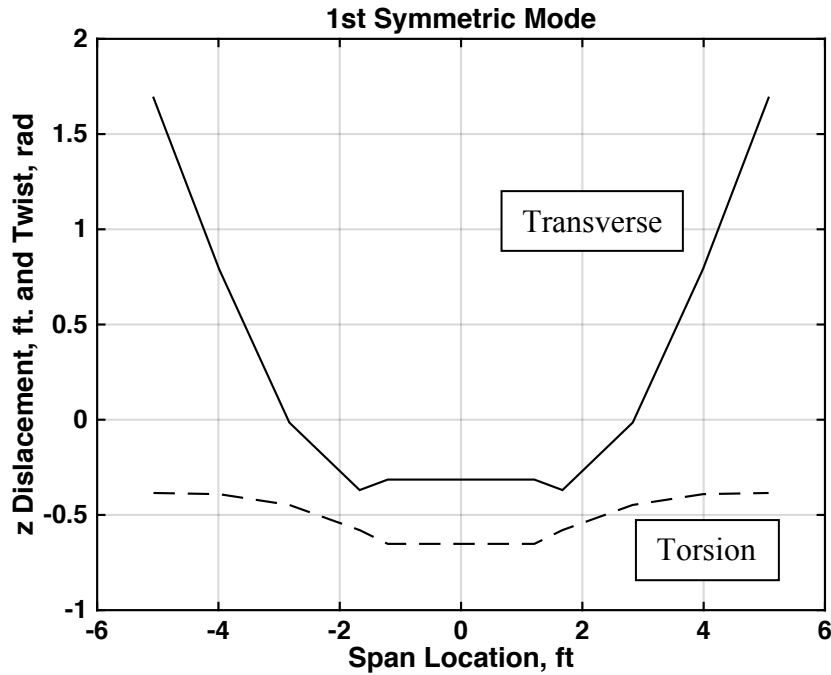

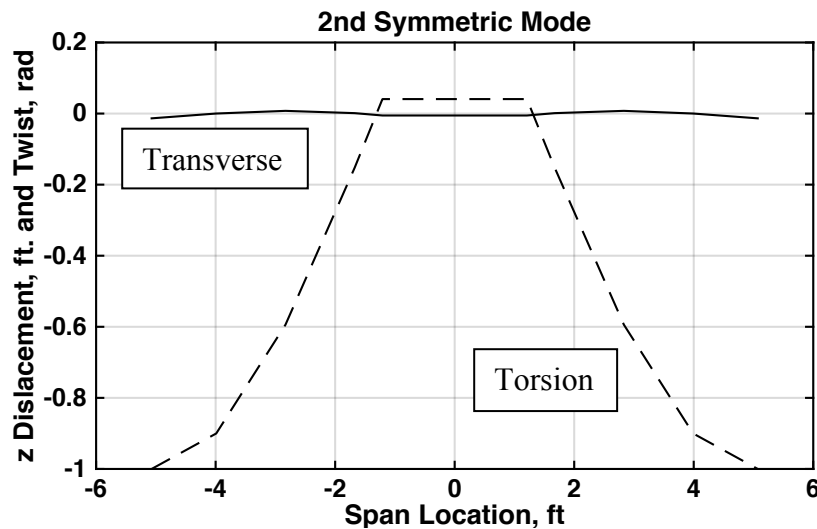**Figure 7, Mode Shape, First Symmetric Mode**

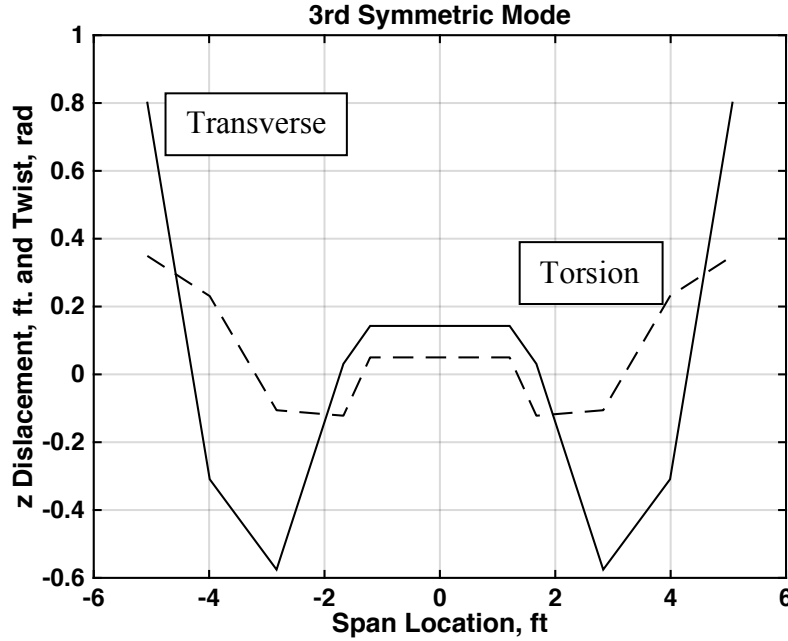**Figure 8, Mode Shape, Second Symmetric Mode**

Figure 9, Mode Shape, Third Symmetric Mode

As noted in Ref. 4, Chapter 2, for example, one can describe the instantaneous shape of the structure in terms of the *n* free-vibration mode shapes and modal coordinates, if *n* is sufficiently large. That is, the instantaneous elastic deformation $\mathbf{d}_E$ of the vehicle's structure at location $\mathbf{p}$ on the undeformed vehicle can be expressed in terms of the *n* vibration mode shapes evaluated at location $\mathbf{p}$, or $\mathbf{v}_i(\mathbf{p})$, and the *n* time-dependent vibration modal coordinates $\eta_i(t)$ as

$$\mathbf{d}_E(\mathbf{p},t) = \sum_{i=1}^{n} \mathbf{v_i}(\mathbf{p})\eta_i(t) \qquad 2$$

When all $\eta_i = 0$, therefore, the vehicle is in its undeformed shape.

The system states associated with these *n* elastic degrees of freedom are initially chosen to be the corresponding free-vibration modal coordinates $\eta_i(t)$. Furthermore, from Lagrange's equation, these *n* modal coordinates are governed by *n* second order differential equations of the following form

$$\ddot{\eta}_i(t) + 2\zeta_i\omega_i\dot{\eta}(t) + \omega_i^2\eta_i = Q_i \,/\, \mathcal{M}_i \qquad 3$$

where ζ_i = vibration modal damping

           ω_i = vibration modal frequency

           Q_i = generalized force acting on the *i*'th modal coordinate

           $\mathcal{M}_i$ = generalized mass of the *i*'th vibration mode

Since one of our research objectives is to develop a relatively low-order dynamic model, we will here include only the first three symmetric modes, or here *n* = 3. We also know from Ref. 1 that at least the first two modes are critical to the flutter characteristics.

8

5. The Aeroelastic Coefficients

The aerodynamic forces and moments on a flight vehicle arise from both rigid-body motion and elastic deformation. Or, as discussed in Ref. 4, Chapters 6 and 7, the vector of aerodynamic forces and moments **F** may be expressed as shown in Eqn. 4. This is consistent with small disturbance theory, and includes the aeroelastic forces.

$$\mathbf{F} = \mathbf{A}_R \mathbf{x}_R + \mathbf{A}_E \mathbf{x}_E + \mathbf{B}_C \mathbf{u} \qquad\qquad 4$$

where $\mathbf{x}_R$ = state vector representing the rigid-body DOF's (u_{rig}, w_{rig} or α_{rig}, θ_{rig}, q_{rig})

          $\mathbf{x}_E$ = state vector consisting of elastic modal coordinates (η_i, $\dot{\eta}_i$ the free-vibration modal coordinates)

          $\mathbf{u}$ = vector of control-surface displacements

          $\mathbf{A}_R$, $\mathbf{A}_E$, $\mathbf{B}_C$ = matrices of dimensional stability derivatives – both rigid-body and aeroelastic

By appropriately partitioning the vector **F** and the matrices above, let's define

$$\mathbf{F} = \begin{bmatrix} \mathbf{F}_R \\ \mathbf{F}_E \end{bmatrix}, \qquad \mathbf{A}_R \triangleq \begin{bmatrix} \mathbf{A}_{RR} \\ \mathbf{A}_{RE} \end{bmatrix}, \qquad \mathbf{A}_E \triangleq \begin{bmatrix} \mathbf{A}_{ER} \\ \mathbf{A}_{EE} \end{bmatrix}, \qquad \mathbf{B}_C \triangleq \begin{bmatrix} \mathbf{B}_R \\ \mathbf{B}_E \end{bmatrix} \qquad\qquad 5$$

Now note that the elements of the matrices $\mathbf{A}_{RR}$ and $\mathbf{B}_R$ are functions of the rigid-body stability derivatives discussed previously, and would already be contained in a flight-dynamics model of the rigid vehicle in its <u>undeformed shape</u>, since $\mathbf{F}_R$ (without the elastic contributions) would be incorporated in that model. The remaining dimensional derivatives in the matrices $\mathbf{A}_{RE}$, $\mathbf{A}_{ER}$, $\mathbf{A}_{EE}$, and $\mathbf{B}_E$ are to be discussed here.

Considering only longitudinal forces and moment F_X, F_Z, and M, and the generalized forces acting on the n symmetric vibration-modal coordinates, the four matrices of interest may be written as

$$\mathbf{A}_{RE} = q_\infty S \bar{c} \begin{bmatrix} C_{Q_{1_u}} & C_{Q_{1_w}} & 0 & C_{Q_{1_q}} \\ \vdots & \vdots & \vdots & \vdots \\ C_{Q_{n_u}} & C_{Q_{n_w}} & 0 & C_{Q_{n_q}} \end{bmatrix}, \quad \mathbf{A}_{ER} = diag\left(q_\infty S, q_\infty S, q_\infty S \bar{c} \right) \begin{bmatrix} C_{X_{\eta_1}} & C_{X_{\dot{\eta}_1}} & \cdots & C_{X_{\eta_n}} & C_{X_{\dot{\eta}_n}} \\ C_{Z_{\eta_1}} & C_{Z_{\dot{\eta}_1}} & \cdots & C_{Z_{\eta_n}} & C_{Z_{\dot{\eta}_n}} \\ C_{M_{\eta_1}} & C_{M_{\dot{\eta}_1}} & \cdots & C_{M_{\eta_n}} & C_{M_{\dot{\eta}_n}} \end{bmatrix}$$

$$\qquad\qquad 6$$

$$\mathbf{A}_{EE} = q_\infty S \bar{c} \begin{bmatrix} C_{Q_{1_{\eta_1}}} & C_{Q_{1_{\dot{\eta}_1}}} & \cdots & C_{Q_{1_{\eta_n}}} & C_{Q_{1_{\dot{\eta}_n}}} \\ \vdots & \vdots & \vdots & \vdots & \vdots \\ C_{Q_{n_{\eta_1}}} & C_{Q_{n_{\dot{\eta}_1}}} & \cdots & C_{Q_{n_{\eta_n}}} & C_{Q_{n_{\dot{\eta}_n}}} \end{bmatrix}, \quad \mathbf{B}_E = q_\infty S \bar{c} \begin{bmatrix} C_{Q_{1_{u_1}}} & \cdots & C_{Q_{1_{u_m}}} \\ \vdots & \vdots & \vdots \\ C_{Q_{n_{u_1}}} & \cdots & C_{Q_{n_{u_m}}} \end{bmatrix}$$

$$\mathbf{A}_{EE} = q_\infty S \bar{c} \begin{bmatrix} C_{Q_{1_{\eta_1}}} & C_{Q_{1_{\dot{\eta}_1}}} & \cdots & C_{Q_{1_{\eta_n}}} & C_{Q_{1_{\dot{\eta}_n}}} \\ \vdots & \vdots & \vdots & \vdots & \vdots \\ C_{Q_{n_{\eta_1}}} & C_{Q_{n_{\dot{\eta}_1}}} & \cdots & C_{Q_{n_{\eta_n}}} & C_{Q_{n_{\dot{\eta}_n}}} \end{bmatrix}, \quad \mathbf{B}_E = q_\infty S \bar{c} \begin{bmatrix} C_{Q_{1_{u_1}}} & \cdots & C_{Q_{1_{u_m}}} \\ \vdots & \vdots & \vdots \\ C_{Q_{n_{u_1}}} & \cdots & C_{Q_{n_{u_m}}} \end{bmatrix}$$

Again as discussed in Ref. 4, Chapter 7, various methods exist to estimate the aeroelastic coefficients appearing in the above four matrices. Integral expressions based on virtual-work concepts are given in that reference for estimating these coefficients, and these integrals are expressed in terms of lifting-surface geometry, the aerodynamic properties of the 2-D airfoil sections, and the free-vibration mode shapes discussed above. Unsteady-aerodynamic effects will be assumed negligible here. If unsteady affects are deemed necessary to more accurately capture the flutter speeds, they may be added at a later time.

Using the integral expressions given in Ref. 4, Chapter 7, plus those given in the Appendix, all evaluated in MATLAB®, the aeroelastic coefficients are given in Table B2 in Section 11, Appendix B. The effect of elastic deformation on the vehicle drag is assumed negligible. Several of the coefficients are inversely proportion to the flight velocity, so for these coefficients the values listed in the table is the coefficient's value multiplied by flight velocity. Finally, the four control deflections $\delta_1 - \delta_4$ correspond to symmetric deflections of control surfaces one through four along the wings, respectively, as shown in Fig. 3. As with the rigid-body aero stability derivatives, no direct comparison between these results and those from LM could be performed, since they were not reported in Ref. 1.

6. The NDOF Model – Model Structure

As noted previously, the first three symmetric vibration modes will be included in the modeling process, and body-freedom flutter and bending-torsion flutter is expected to involve at least the first two of these elastic degrees of freedom. The resulting state-variable model takes the form given in Eqns. 7 below, with the first four states corresponding to the three rigid-body degrees of freedom, while the last six states correspond to the three elastic degrees of freedom. Note that the states associated with the rigid-body degrees of freedom are identical to those in the rigid-body model presented previously. That is, in the longitudinal axes the first four states are surge velocity u_{rig}, vehicle angle of attack α_{rig}, vehicle pitch attitude θ_{rig}, and vehicle pitch rate q_{rig}, which describe the motion of the vehicle-fixed frame or mean axes (see Ref. 4, Chapter 4 for definitions). Consequently, the state vector is composed of purely rigid-body and elastic states, and note the natural partitioning of the system into rigid-body and elastic subsystems. The **A**-matrix partitioning indicated below is related, but not identical to that given in Eqn. 5. In the rows of the A and B matrices corresponding to the elastic degrees of freedom, the terms denoted as Z_η, M_η, and $\Xi_.$ are the dimensional aeroelastic derivatives found from the aeroelastic coefficients given in Table B2 in Section 11, Appendix B.

7. Flutter Analysis

Now consider Fig. 9, showing the dynamic-pressure root locus for the system **A** matrix just described. The eigenvalue locations are shown for seven flight velocities between 30 and 60 kt (51–101 fps). The system modes are labeled according to their modal genesis. That is, the mode branches are identified according to their genesis mode of pure rigid-body mode or pure free-vibration mode with no aerodynamic forces. But to be clear, all the modes involve coupling through the aerodynamics, and hence are not pure short period, pure bending-torsion vibration, etc.

$$\mathbf{x}^T = \begin{bmatrix} u_{rig} & \alpha_{rig} & \theta_{rig} & q_{rig} & \vdots & \eta_1 & \dot{\eta}_1 & \eta_2 & \dot{\eta}_2 & \eta_3 & \dot{\eta}_3 \end{bmatrix}$$

$$\mathbf{A} = \left[\begin{array}{cccc:cccccc}
X_u & X_\alpha & -g & X_q & 0 & 0 & \cdots & 0 & 0 \\
Z_u/U_0 & Z_\alpha/U_0 & 0 & 1+Z_q/U_0 & Z_{\eta_1}/U_0 & Z_{\dot{\eta}_1}/U_0 & \cdots & Z_{\eta_3}/U_0 & Z_{\dot{\eta}_3}/U_0 \\
0 & 0 & 0 & 1 & 0 & 0 & \cdots & 0 & 0 \\
M_u & M_\alpha & 0 & M_q & M_{\eta_1} & M_{\dot{\eta}_1} & \cdots & M_{\eta_3} & M_{\dot{\eta}_3} \\
\hdashline
0 & 0 & 0 & 0 & 0 & 1 & \cdots & 0 & 0 \\
0 & \Xi_{1_\alpha} & 0 & \Xi_{1_q} & \Xi_{1_{\eta_1}}-\omega_1^2 & \Xi_{1_{\dot{\eta}_1}}-2\zeta_1\omega_1 & \cdots & \Xi_{1_{\eta_3}} & \Xi_{1_{\dot{\eta}_3}} \\
\vdots & \vdots & \vdots & \vdots & \vdots & \vdots & \cdots & \vdots & \vdots \\
0 & 0 & 0 & 0 & 0 & 0 & \cdots & 0 & 1 \\
0 & \Xi_{3_\alpha} & 0 & \Xi_{3_q} & \Xi_{0_{\eta_1}} & \Xi_{3_{\dot{\eta}_1}} & \cdots & \Xi_{3_{\eta_3}}-\omega_3^2 & \Xi_{3_{\dot{\eta}_3}}-2\zeta_3\omega_3
\end{array} \right]$$

7

$$\mathbf{A} = \left[\begin{array}{c:c} \mathbf{A}_{RR} & \mathbf{A}_{RE} \\ \hdashline \mathbf{A}_{ER} & \mathbf{A}_{EE} \end{array} \right] \qquad \mathbf{B} = \begin{bmatrix} X_{\delta_1} & \cdots & X_{\delta_4} \\ Z_{\delta_1}/U_0 & \cdots & Z_{\delta_4}/U_0 \\ 0 & \cdots & 0 \\ M_{\delta_1} & \cdots & M_{\delta_4} \\ \hdashline 0 & \cdots & 0 \\ \Xi_{1_{\delta_1}} & \cdots & \Xi_{1_{\delta_4}} \\ 0 & \cdots & 0 \\ \Xi_{2_{\delta_1}} & \cdots & \Xi_{2_{\delta_4}} \\ 0 & \cdots & 0 \\ \Xi_{3_{\delta_4}} & \cdots & \Xi_{3_{\delta_4}} \end{bmatrix} = \begin{bmatrix} \mathbf{B}_R \\ \hdashline \mathbf{B}_E \end{bmatrix}$$

Now consider the branch labeled "Short Period." As the flight velocity, or dynamic pressure, increases, the roots move away from the origin, as in the rigid-body case shown in Fig. 5. But here they move farther into the left-half plane. The next branch labeled "1st Bending" begins at the pole from the first symmetric-bending vibration mode, almost on the imaginary axis at 34.6 rad/sec (the vibration frequency), and initially moves further into the left-half plane for the lower flight velocities. As flight velocity continues to increase, this branch loops back around to the right and eventually crosses the imaginary axis. This axis crossing corresponds to the flutter condition known as body-freedom flutter (BFF), and for this model BFF occurs at a flight velocity of approximately 47 kt (78 fps) and with a flutter frequency of 27.5 rad/sec (4.4 Hz). Body-freedom flutter is a unique aeroelastic phenomenon that involves interactions between the rigid-body and elastic DOFs, or the "short-period" and the "first-bending" modes here. This flutter phenomenon was first discovered on forward-swept wing aircraft like the X-29 (Ref. 13).
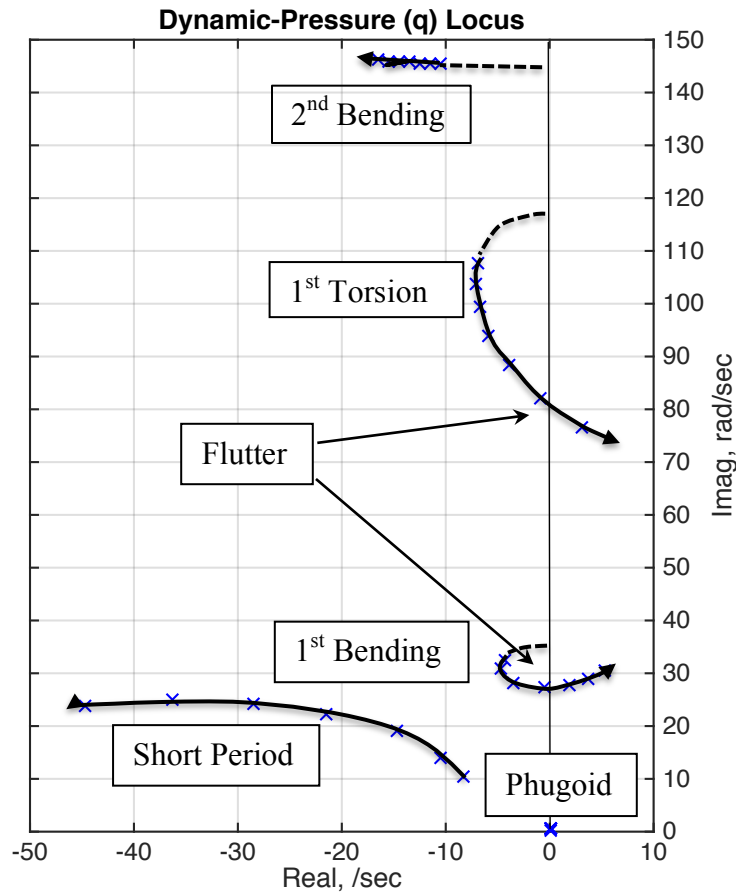
Figure 9, Dynamic-Pressure Root Locus

Next, with regard to the branch labeled "1st Torsion," it begins at the pole arising from the second symmetric vibration mode, almost on the imaginary axis at 117.8 rad/sec, and also begins moving into the left-half plane. As flight velocity continues to increase, it also curves back to the right and crosses the imaginary axis, indicating another flutter mode involving the first-bending and first-torsion modes. This flutter condition, as modeled, occurs at a flight velocity of approximately 57 kt (65.5 fps), and with a flutter frequency of 80 rad/sec (12.7 Hz).

Finally, consider the branch labeled "2nd Bending. This branch begins near the imaginary axis at 145.6 rad/sec, this mode's vibration frequency, and as the flight velocity increases, these roots simply move further into the left half plane. The phugoid roots remain near the origin at all flight velocities.

Some variations on the above model were also considered, which involve truncating or residualizing the second and/or third elastic degrees of freedom. (Recall that in residualization, the velocities of the residualized states are set to zero, and these states are then eliminated algebraically.) Residualization yields a reduced-order model that retains the static-elastic effects of the residualized degrees of freedom on the aerodynamics, while truncation eliminates both the dynamics and the static-elastic aerodynamic effects of the truncated degrees of freedom.

First, neither truncation nor residualization of the third elastic degree of freedom alone had a major effect on the flutter results. The main result was slight modifications of the dampings of the retained aeroelastic DOFs, while slightly affecting the flutter speeds. The

conclusion here is that this third elastic degree of freedom has a small but measurable effect on the flutter characteristics.

However, truncation or residualization of both the second and third elastic degrees of freedom leads to quite different results. Considering the dynamic-pressure, or *q*, root loci in Fig. 10, the *q* root locus for the original 10th order model is again shown by the solid lines, but the imaginary axis has a maximum value of only 50 rad/sec, not showing the first-torsion or second-bending branches, to enlarge the low-frequency region of the complex plane. The *q* locus for the truncated model is also shown by the dashed lines for 40, 45, and 50 kt, while the locus for the residualized model is shown by the dotted lines for the same velocities. As can be noted, the *q* locus for the truncated model is quite different from the other two, and is very similar to that for the rigid vehicle (Fig. 5), except for the additional aeroelastic mode here. Neither the "Short-Period" nor the "1st Bending" roots move as much with flight velocity, and no flutter instability is indicated over this range of velocities. So the "Short-Period" and "1st-bending" modes appear to interact much less in the absence of the "1st Torsion" mode.
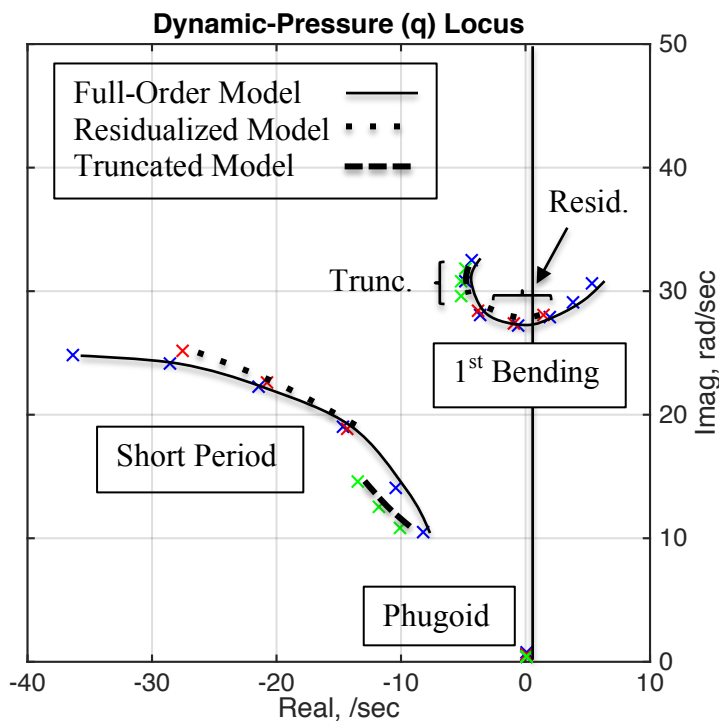
Figure 10, Comparison of the *q* Loci

In contrast, the *q* root locus for the residualized model (dotted lines) is quite similar to that for the full-order model. There again exists considerable interaction between the "Short-Period" and "1st Bending" modes, and this residualized model also suggests BFF occurs at a flight velocity of approximately 47 kt (79 fps) with a flutter frequency of 27.5 rad/sec. These results are almost identical to those obtained from the 10th-order model for the BFF condition, and these combined results also indicate that the static-elastic effects of the first-torsion mode, included in the residualized model, are important to the existence of BFF here.

When comparing all these results with LM's analytical results reported in Ref. 1, we find quite good agreement in terms of the presence of the two flutter conditions, and with regards to the flutter speeds, flutter frequencies, and genesis modes of the flutter conditions. Plus, the flight-

test results reported in Ref. 1 confirmed a critical flutter speed of approximately 46 kts, or 77.7 fps, which again agrees quite well with the BFF condition indicated by both our full-order and residualized models. In addition, as with the LM modeling, our full-order model indicates a 57 kt flutter speed along with a 12.7 Hz flutter frequency for the bending-torsion flutter mode. All these results are summarized in Table 2 below.

Table 2, Comparison Of Flutter Speeds and Frequencies

Model/Test	BFF Flutter Speed	BFF Flutter Frequency	BT Flutter Speed	BT Flutter Frequency
LM Analytical	43 kt	4.2 Hz	57 kt	10.5 Hz
LM Flight Test	46 kt	4.5 Hz	NA	NA
Full-Order Model	47 kt	4.4 Hz	57 kt	12.7 Hz
Residualized Model	47 kt	4.4 HZ	NA	NA
Truncated Model	No Flutter	No Flutter	NA	NA

An additional comparison with the Lockheed Martin (LM) results is shown in Fig. 11. A velocity-frequency-damping (VFG) plot is shown, taken from Ref. 1, which indicates the frequencies and damping ratios of the system modes, plotted versus flight velocity. This plot shows LM's analytical results for both the symmetric (longitudinal) and anti-symmetric (lateral-directional) modes, but we are only concerned with the symmetric modes and the longitudinal axis. The results from our full-order model are also indicated in this plot by the dots in colors matching the corresponding curves shown in the VFG plot, at several selected flight velocities.
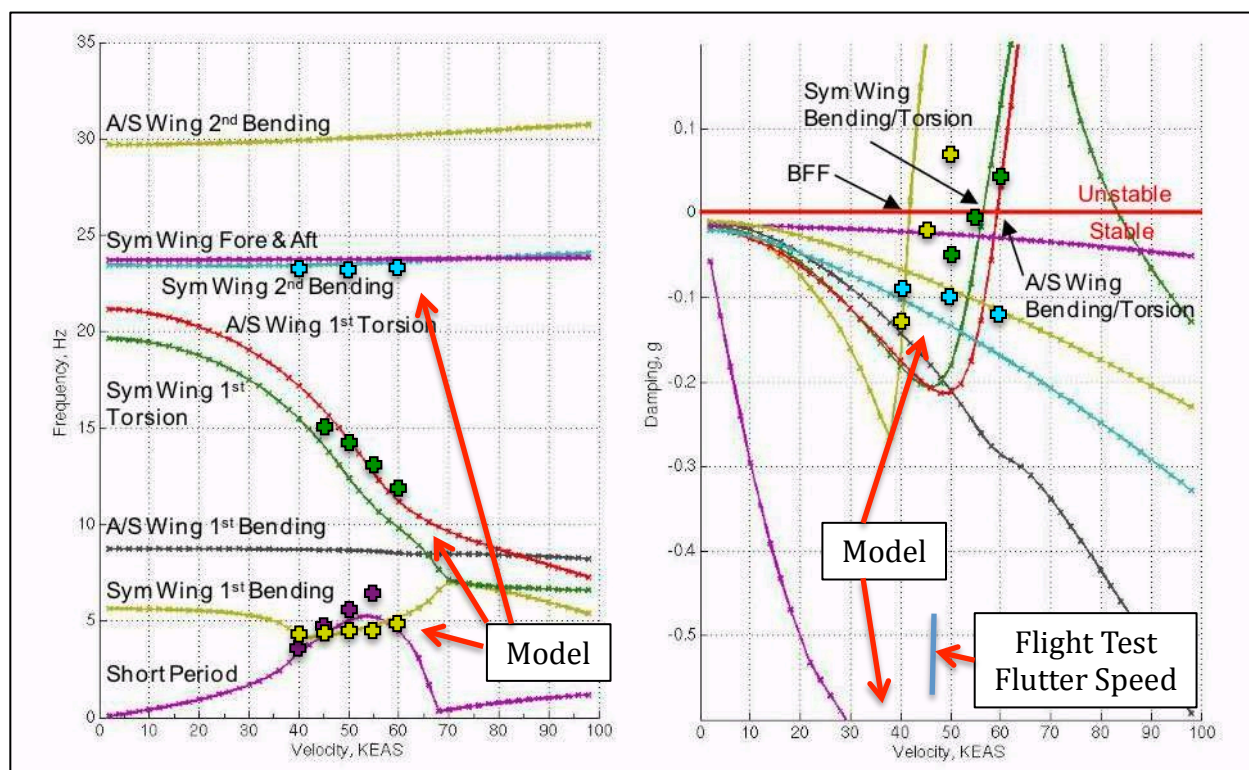
Figure 11, VFG Flutter-Plot Comparison

These model-based results agree quite well in terms of the flutter speeds, and in terms of both frequency and damping of the three longitudinal modes – "Short Period," "1st Bending," and "1st Torsion." And the predicted BFF flutter speeds of about 47 kt agrees even better with the flight-test results, which indicated a flutter speed of 46 kt, slightly higher than suggested by LM's analytical results.

Any differences between the results from our models and those from Lockheed Martin could be attributed to many factors. Of course, the modeling methodologies probably differ, as discussed at the outset, and unsteady-aerodynamic effects have been ignored here. But the data upon which the models are based also likely differ, and most of this data could not be directly compared. For example, we are not able to compare our rigid-body aerodynamics or the mode shapes and generalized masses of the vibration modes with LM's. Plus, there are some differences between the free-vibration frequencies used in the modeling. In spite of this fact, and of the simplicity of the model presented here, the agreement with LM's results is quite good.

8. Flight Dynamics Analysis

The transfer functions for the pitch attitude and plunge acceleration (measured at the vehicle's *cg* on the center-body centerline) from elevator (δ_3) are given in Eqns. 8 for the full-order model.

$$\frac{\theta_{cg}(s)}{-\delta_3(s)} = \frac{65.24\ [0.0536][7.044][0.22,41.2][0.05,101.7][0.05,165.3]}{[-0.01,0.61][0.59,18.1][0.15,30.9][0.07,103.7][0.08,146.0]}\ \text{deg/deg}$$

$$\frac{n_{Z-cg}(s)}{-\delta_3(s)} = \frac{-0.2276\ [0][-0.0279][29.58][-25.58][0.24,42.3][0.07,104.1][-282.6][246]}{[-0.01,0.61][0.59,18.1][0.15,30.9][0.07,103.7][0.08,146.0]}\ \text{ft/sec}^2\text{/deg}$$

8

The flight condition is 3000 ft altitude and 60 fps velocity, below the BFF flutter speed. These two dynamic responses include the effects of dynamic elastic deformations at that point on the structure corresponding to the *cg* location of the undeformed vehicle. When comparing these transfer functions with those for the rigid vehicle given in Eqns. 1, note that the system is now 10th order, instead of fourth, and the modal frequency and damping ratio of the second mode (originally the short-period mode) have been modified. Also, the zeros in both transfer functions, corresponding to those in Eqns. 1, have been affected. In particular, $1/T_{\theta_1} = 0.054$ /sec and $1/T_{\theta_2} = 7.04$ /sec. Since $1/T_{\theta_2}$ is roughly proportional to the lift effectiveness Z_α, we see that the lift effectiveness has been increased due to the wing twisting. This will be discussed further later in this section. The presence of the aeroelastic modes is indicated by the three sets of higher-frequency dipoles (pole-zero pairs) in each of these transfer functions. The two "highest-frequency" zeros in the acceleration transfer function are effectively at infinity in the complex plane.

The second mode, with a natural frequency of around 18 rad/sec, corresponds to the short-period mode of the rigid vehicle. However, it is no longer a classical short-period mode. This mode's eigenvector (or mode shape), after a state transformation that non-dimensionalizes the surge velocity u ($= u/U_0$) and converts the elastic states to elastic pitch deformation (twist) measured at the vehicle centerline θ_{E1}, θ_{E2}, and θ_{E3}, is depicted in Fig. 12. Note that unlike the conventional short-period mode shape for the rigid vehicle in Fig. 4, the second largest

15

contributor to this modal response is the elastic-pitch-rate displacement associated with the first aeroelastic degree of freedom $\dot{\theta}_{E1}$. For the rigid vehicle this component is of course absent in the short-period modal response, and the second largest contributors are rigid-body angle of attack α_{rig} and pitch attitude θ_{rig}. So as in a true short-period mode, there is virtually no surge velocity u_{rig} present in the mode shape, the mode is dominated by the rigid-body pitch-rate response of the vehicle q_{rig}, and the phase relationships between pitch rate, pitch attitude, and angle of attack are as in the conventional short-period mode. But this mode is a coupled rigid-body and elastic mode.
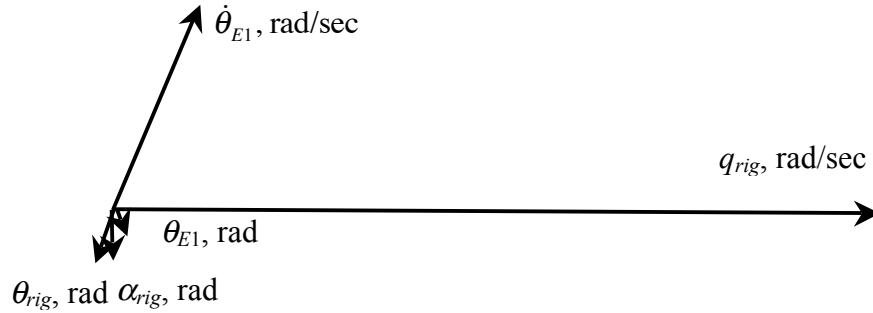
Figure 12, "Elastic Short-Period" Mode Eigenvector (Mode Shape)

The next-highest-frequency mode reflected in the transfer functions is the lightly damped first aeroelastic mode (AE Mode 1), with an undamped natural frequency of approximately 31 rad/sec. This mode's eigenvector (or mode shape) is depicted in Fig. 13. This mode is also a coupled rigid-body/elastic mode, but is dominated by the elastic-pitch-rate deformation at the vehicle's center body associated with the first elastic (bending-torsion) degree of freedom, $\dot{\theta}_{E1}$.
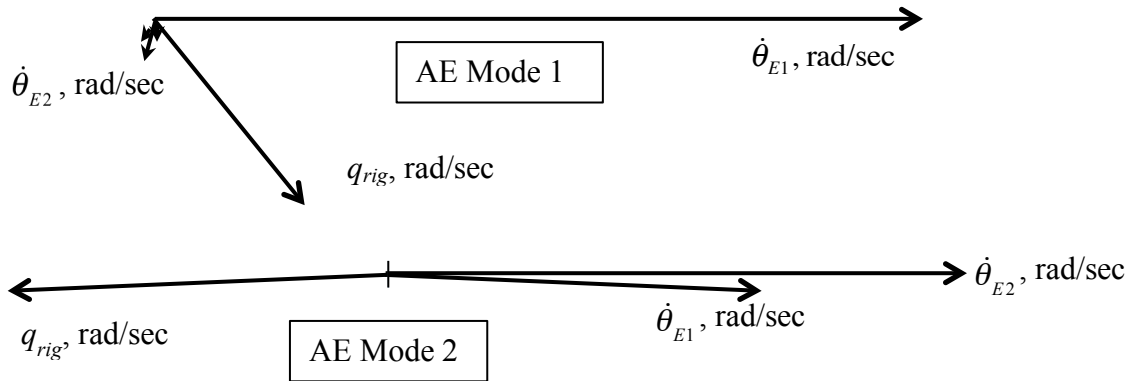
Figure 13, Coupled First and Second Aeroelastic Mode Eigenvectors (Mode Shapes)

The next largest contributor to this modal response is the rigid-body pitch rate (or the pitch rate of the mean axis of the vehicle) q_{rig}. And the next largest contributor after that is elastic pitch rate of the center body associated with the second elastic degree of freedom $\dot{\theta}_{E2}$. There are also small contributions from the rigid-body angle of attack and pitch attitude, but they are so small that they are difficult to display in the figure, and there is again virtually no surge velocity u_{rig} present in this modal response. So as with the elastic-short-period mode in Fig. 12, this first

aeroelastic mode exhibits rigid-elastic coupling, leading to the body-freedom-flutter condition at higher flight velocity.

The next-highest-frequency mode here is the second aeroelastic mode (AE Mode 2), with an undamped natural frequency of approximately 104 rad/sec. This mode's eigenvector (or mode shape) is also depicted in Fig. 13. Recall the genesis of this mode was a purely torsional vibration mode. This mode is now also a coupled rigid-body/elastic mode, but is dominated by the elastic pitch-rate deformation of the vehicle's center body associated with the second elastic degree of freedom $\dot{\theta}_{E2}$. The next largest contributors to this modal response are the rigid-body pitch rate q_{rig} and the elastic pitch rate of the center body associated with the first elastic degree of freedom $\dot{\theta}_{E1}$. The remaining contributors are so small that they are difficult to display in the figure, and there is virtually no surge velocity u_{rig} present in this modal response either. It is interesting to note that in this modal response the elastic-pitch-rate deformation associated with the first two elastic degrees of freedom $\dot{\theta}_{E1}$ and $\dot{\theta}_{E2}$ are almost perfectly in phase, while the rigid-body pitch rate q_{rig} is out of phase with these two responses. Again this second aeroelastic mode exhibits rigid-elastic coupling, and it is this coupling that also contributes to the existence of the body-freedom-flutter condition at higher flight velocity.

The last mode is the third aeroelastic mode (mode shape not plotted) with an undamped frequency of 146 rad/sec, and it is entirely dominated by elastic pitch-rate deformation associated with the third elastic degree of freedom, or $\dot{\theta}_{E3}$. There are only slight contributions due to $\dot{\theta}_{E1}$ and $\dot{\theta}_{E2}$, as well as q_{rig}. So this is almost a pure aeroelastic mode.

The Bode plot of the pitch rate from (negative) elevator deflection, measured at the point on the structure corresponding to the *cg* location of the undeformed vehicle are shown by the solid lines in Fig. 14. The flight velocity in this case is 40 kts, or 68 fps. The magnitude and phase contributions from the well-damped short-period-like mode near 18 rad/sec merges with those from the first aeroelastic mode near 31 rad/sec. The two dipoles associated with the lightly-damped aeroelastic modes near 104 and 146 rad/sec are also evident.
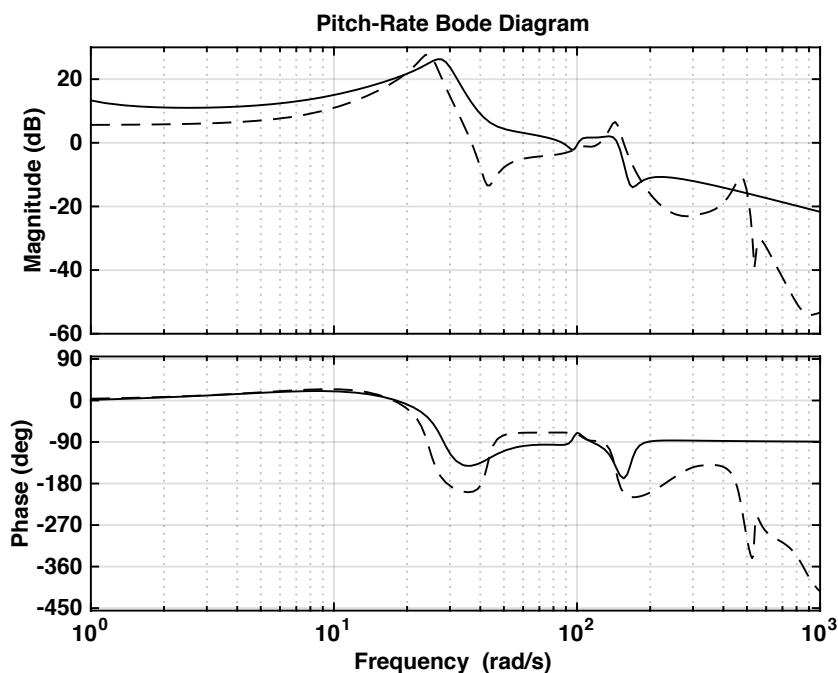

Pitch-Rate Bode Diagram

Figure 14, Bode Plot – Pitch Rate (q_{cg}) From Negative Elevator (deg/sec/deg)

Also shown for reference in Fig. 14 is the same pitch-rate response, but from a linear model provided by Lockheed Martin corresponding to the results given in Ref.1. This model of the bare airframe (no actuator or sensor dynamics) includes the effects of unsteady aerodynamics. It is noted that the elevator control power agrees well between the models, as evidenced by the good agreement in the Bode magnitudes. Also evident is the presence of a pole-zero dipole between 20 and 42 rad/sec, which agrees with the model presented in this paper, except the complex zeros in the Lockheed-Martin model are closer to the imaginary axis leading to a more pronounced phase increase around 40 rad/sec. But in general there is good agreement between the two models below 146 rad/sec. The Lockheed Martin model includes additional aeroelastic modes above that frequency.

As a final topic, we will derive and discuss another reduced-order model of the elastic vehicle. This model is obtained by residualizing all three elastic degrees of freedom, yielding a model for the dynamics of the rigid-body degrees of freedom only, but including the effects of static displacements of the elastic degrees of freedom by adjusting the aerodynamic stability derivatives. This model represents the "rigid-body" dynamics of the vehicle in its in-flight shape under load, as opposed to the model in Section 3 that reflects the dynamics of the vehicle in its undeformed or rigid shape. The differences between the stability derivatives in these two models represent measures of the flexibility of the structure.

The adjusted aerodynamic stability derivatives for the residualized model are obtained as follows (Ref. 4, Section 7.11). Consistent with Eqns. 7, consider the linearized equations of motion for the longitudinal dynamics written in the following form:

$$\dot{\mathbf{x}}_R = \mathbf{A}_{0R}\mathbf{x}_R + \mathbf{A}_{RR}\mathbf{x}_R + \begin{bmatrix} \mathbf{A}_{R\eta} & \mathbf{A}_{R\dot{\eta}} \end{bmatrix}\mathbf{x}_E + \mathbf{B}_R\mathbf{u}$$

$$\dot{\mathbf{x}}_E = \begin{bmatrix} \mathbf{0} \\ \mathbf{A}_{ER} \end{bmatrix}\mathbf{x}_R + \begin{bmatrix} \mathbf{0} & \mathbf{I} \\ \mathbf{A}_{0\eta} & \mathbf{A}_{0\dot{\eta}} \end{bmatrix}\mathbf{x}_E + \begin{bmatrix} \mathbf{0} & \mathbf{0} \\ \mathbf{A}_{E\eta} & \mathbf{A}_{E\dot{\eta}} \end{bmatrix}\mathbf{x}_E + \mathbf{B}_E\mathbf{u}$$

(9)

where the rigid-body and elastic states, control inputs, etc. are given as

$$\mathbf{x}_R = \begin{Bmatrix} u_{rig} \\ \alpha_{rig} \\ \theta_{rig} \\ q_{rig} \end{Bmatrix}, \quad \mathbf{x}_E = \begin{Bmatrix} \eta \\ \dot{\eta} \end{Bmatrix} = \begin{Bmatrix} \eta_1 \\ \eta_2 \\ \eta_3 \\ \dot{\eta}_1 \\ \dot{\eta}_2 \\ \dot{\eta}_3 \end{Bmatrix}, \quad \mathbf{u} = \begin{Bmatrix} \delta_1 \\ \delta_2 \\ \delta_3 \\ \delta_4 \end{Bmatrix}, \quad \mathbf{A}_{0R} = \begin{bmatrix} 0 & 0 & -g & 0 \\ 0 & 0 & 0 & 1 \\ 0 & 0 & 0 & 1 \\ 0 & 0 & 0 & 0 \end{bmatrix}$$

(10)

$$\mathbf{A}_{0\eta} = \begin{bmatrix} -\omega_1^2 & 0 & 0 \\ 0 & -\omega_2^2 & 0 \\ 0 & 0 & -\omega_3^2 \end{bmatrix}, \quad \mathbf{A}_{0\dot{\eta}} = \begin{bmatrix} -2\zeta_1\omega_1 & 0 & 0 \\ 0 & -2\zeta_2\omega_2 & 0 \\ 0 & 0 & -2\zeta_3\omega_3 \end{bmatrix}$$

The elements of the remaining matrices are dimensional stability derivatives such as M_α in the aerodynamic model for the forces, moments, and generalized forces.

Setting the elastic-rates to zero, and solving for the static-elastic displacements we have

$$\boldsymbol{\eta}_o = -\left(\mathbf{A}_{0\eta} + \mathbf{A}_{E\eta}\right)^{-1}\left(\mathbf{A}_{ER}\mathbf{x}_R + \mathbf{B}_E\mathbf{u}\right) \tag{11}$$

And after substituting this constraint back into the EOM's we have the residualized reduced-order model (ROM) given by

$$\dot{\mathbf{x}}_R = \mathbf{A}_{0R}\mathbf{x}_R + \left(\mathbf{A}_{RR} - \mathbf{A}_{R\eta}\left(\mathbf{A}_{0\eta} + \mathbf{A}_{E\eta}\right)^{-1}\mathbf{A}_{ER}\right)\mathbf{x}_R + \left(\mathbf{B}_R - \mathbf{A}_{R\eta}\left(\mathbf{A}_{0\eta} + \mathbf{A}_{E\eta}\right)^{-1}\mathbf{B}_E\right)\mathbf{u}$$
$$= \mathbf{A}_{ROM}\mathbf{x}_R + \mathbf{B}_{ROM}\mathbf{u} \tag{12}$$

The dimensional aerodynamic derivatives adjusted for static-elastic deflections are then the elements of

$$\left(\mathbf{A}_{RR} - \mathbf{A}_{R\eta}\left(\mathbf{A}_{0\eta} + \mathbf{A}_{E\eta}\right)^{-1}\mathbf{A}_{ER}\right) \text{ and } \left(\mathbf{B}_R - \mathbf{A}_{R\eta}\left(\mathbf{A}_{0\eta} + \mathbf{A}_{E\eta}\right)^{-1}\mathbf{B}_E\right) \tag{13}$$

The resulting adjusted non-dimensional aerodynamic coefficients for our vehicle are then listed in Table B3 in Section 11, Appendix B.

When one compares the aero derivatives in Table B3 with those for the rigid vehicle in Table B1, several large differences may be noted. And these differences of course, are due to the static deformation of the structure. Consider, for example, the effect of angle of attack on the lift and pitching moment, or C_{L_α} and C_{M_α}. As the angle of attack increases, the bending moment on the wing increases, which tends to bend the flexible wing. But from the mode shape of the lowest-frequency first symmetric mode in Fig. 7, as the wing bends up it also twists leading-edge up. And this further increases the angle of attack of the wing. The effect is to drastically increase the effect of vehicle angle of attack on lift and pitching moment. Similar analyses help explain the changes in effectiveness of the control surfaces, for example. Surface deflections not only increase the wing lift due to changes in camber, but also twist it. Fortunately, however, no static control reversals are indicated in the data. That is, all positive control deflections increase vehicle lift and induce a negative pitching moment. But it should be clear from these results that this vehicle is very flexible with quick attitude response. And the effects of flexibility make the pitch response even faster.

The pitch-rate and plunge acceleration transfer functions from this residualized reduced-order model at 60 fps, corresponding to Eqns. 1 and 8, are

$$\frac{\theta_{cg}(s)}{-\delta_3(s)} = \frac{1047\,[0.0404][8.431]}{[-0.01, 0.61][0.65, 16.9]} \text{ deg/deg}$$

$$\tag{14}$$

$$\frac{n_{Z-cg}(s)}{-\delta_3(s)} = \frac{1.20\,[0][-0.0279][28.73][-27.02]}{[-0.01, 0.61][0.65, 16.9]} \text{ fps/deg}$$

Clearly these transfer functions differ significantly from those given in Eqns. 1 for the rigid vehicle. The short-period damping and frequency differ due to the changes in effective C_{M_α} and C_{M_q}, and $1/T_{\theta 2}$ is increased due to the increase in C_{L_α}.

A final comparison between the three models we've developed is given in Fig. 15, which includes the pitch-rate step responses from negative elevator deflection plotted in deg/sec/deg.

The "Rigid Model" response corresponds to Eqns. 1, the "Static-Elastic Corrected" response is the response from the residualized reduced-order model being discussed here, and the "Full-Order" response is from the full-order model, or Eqns. 8. These responses differ significantly, indicating the degree of flexibility in this vehicle. Comparing the first two responses reveals the effects of the <u>static-elastic</u> deflections of the structure, while comparing the last two responses reveals the effects of the <u>dynamic</u> response of the structure.
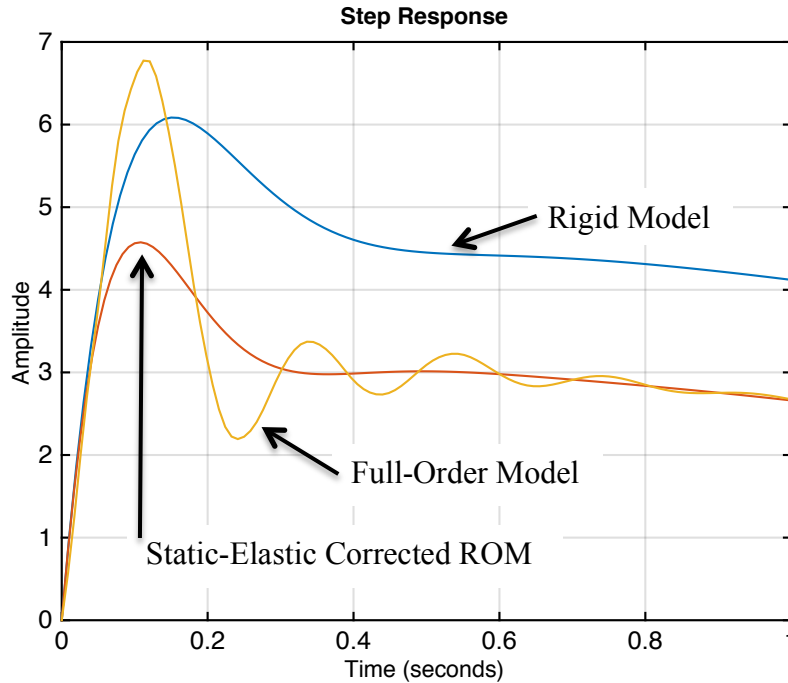
Figure 15, Pitch-Rate Step Response From Del3 (deg/sec/deg)

9. Conclusions

A relatively low order linear, semi-analytical model was developed for the longitudinal dynamics of a flexible flying-wing research drone aircraft. The rigid-body degrees of freedom were defined in terms of the motion of the vehicle-fixed coordinate frame (mean axes), as required for flight-dynamics analysis, and the analytical modeling utilized the vibration solution for the vehicle structure obtained from a simple finite-element model. The rigid-body aerodynamic coefficients were obtained from classical, semi-empirical techniques, and the aeroelastic stability derivatives (influence coefficients) were derived from quasi-steady strip theory and virtual work. All numerical analyses, except for estimating the rigid-body aerodynamics, were performed in MATLAB®. The state variables used in the models include the same as those used in modeling a rigid vehicle, plus additional states associated with the elastic degrees of freedom. This model structure helped to provide insight and transparency in the modeling and in the interpretation of results.

It was shown that in spite of the model's relative simplicity, the body-freedom and bending-torsion flutter speeds, frequencies, and genesis modes suggested by this model agreed quite well with the analytical predictions and flight test-results reported by Lockheed Martin. It was also demonstrated that the second symmetric vibration mode appears to be an important

contributor to body-freedom flutter. As modeled, the longitudinal dynamics of the vehicle are characterized by a slightly unstable phugoid mode, a well-damped, pitch-dominated, elastic-short-period mode, and two aeroelastic modes that may be unstable. The elastic-short-period and aeroelastic modes involve significant coupling between the rigid-body and elastic degrees of freedom, as indicated by their mode shapes. Hence, a classical, rigid-body short-period mode does not exist. Furthermore, it is clear from the results that this vehicle is very flexible with quick attitude response. And the effects of flexibility make the pitch response even faster.

10. Acknowledgements

11. Appendices

Appendix A - Vehicle Data

Table A1, Vehicle Mass Properties

Property	Value
Total Weight	12.0 lb
C.G. Location	23.26 in (from nose)
Pitch Moment of Inertia	1245.8 lb-in^2
Roll Moment of Inertia	8529.5 lb-in^2
Yaw Moment of Inertia	8118.4 lb-in^2
Product of Inertia (est)	-0.30 ln-in^2

Table A2, Planform Parameters

Planform Area, S	Span, b	Aspect Ratio, AR	Taper Ratio, λ	M.A.C., $\bar{c}$	LE Sweep, Λ_{LE}
11.67 ft^2	10 ft	8.57	0.425	1.313 ft	22 deg

Appendix B - Aerodynamic and Aeroelastic Coefficient Data

Table B1, Rigid-Body Longitudinal Stability Derivatives

C_{L_α} /rad	C_{M_α} /rad	C_{L_q} sec	C_{M_q} sec	$C_{L_{\delta_1}}$ /rad	$C_{M_{\delta_1}}$ /rad
4.074	-0.310	2.657	-3.830	0.774	-0.014*
$C_{L_{\delta_2}}$ /rad	$C_{M_{\delta_2}}$ /rad	$C_{L_{\delta_3}}$ /rad	$C_{M_{\delta_3}}$ /rad	$C_{L_{\delta_4}}$ /rad	$C_{M_{\delta_4}}$ /rad
0.630	-0.246	0.530	-0.410	0.301	-0.353
C_{D_α} /rad	$C_{D_{\delta_1}}$ /rad	$C_{D_{\delta_2}}$ /rad	$C_{D_{\delta_3}}$ /rad	$C_{D_{\delta_4}}$ /rad	
0.129	0.0012	0.0015	0.0018	0.0012	

* From UMN UAV Lab

Table B2, Aeroelastic Coefficients

$C_{L_{\eta_1}}$	$C_{L_{\dot\eta_1}}$ V∞ (ft)	$C_{M_{\eta_1}}$	$C_{M_{\dot\eta_1}}$ V∞ (ft)	$C_{Q_{1_\alpha}}$	$C_{Q_{1_q}}$ V∞ (ft)	$C_{Q_{1_{\delta_1}}}$	$C_{Q_{1_{\delta_2}}}$
3.0018	-0.6221	-0.0138	1.4328	1.0025	1.4359	-0.3899	-0.1402
$C_{Q_{1_{\delta_3}}}$	$C_{Q_{1_{\delta_4}}}$	$C_{Q_{1_{\eta_1}}}$	$C_{Q_{1_{\eta_2}}}$	$C_{Q_{1_{\eta_3}}}$	$C_{Q_{1_{\dot\eta_1}}}$ V∞ (ft)	$C_{Q_{1_{\dot\eta_2}}}$ V∞ (ft)	$C_{Q_{1_{\dot\eta_3}}}$ V∞ (ft)
0.1076	0.4524	0.2877	1.3324	-0.3901	-1.8350	0.0070	-0.2397
$C_{L_{\eta_2}}$	$C_{L_{\dot\eta_2}}$ V∞ (ft)	$C_{M_{\eta_2}}$	$C_{M_{\dot\eta_2}}$ V∞ (ft)	$C_{Q_{2_\alpha}}$	$C_{Q_{2_q}}$ V∞ (ft)	$C_{Q_{2_{\delta_1}}}$	$C_{Q_{2_{\delta_2}}}$
2.0552	0.0102	-1.1107	-0.0005	0.3499	0.2501	0.0067	0.0019
$C_{Q_{2_{\delta_3}}}$	$C_{Q_{2_{\delta_4}}}$	$C_{Q_{2_{\eta_1}}}$	$C_{Q_{2_{\eta_2}}}$	$C_{Q_{2_{\eta_3}}}$	$C_{Q_{2_{\dot\eta_1}}}$ V∞ (ft)	$C_{Q_{2_{\dot\eta_2}}}$ V∞ (ft)	$C_{Q_{2_{\dot\eta_3}}}$ V∞ (ft)
0.0063	0.0027	0.1398	0.2972	-0.0491	-0.2620	-0.075*	0.0544
$C_{L_{\eta_3}}$	$C_{L_{\dot\eta_3}}$ V∞ (ft)	$C_{M_{\eta_3}}$	$C_{M_{\dot\eta_3}}$ V∞ (ft)	$C_{Q_{3_\alpha}}$	$C_{Q_{3_q}}$ V∞ (ft)	$C_{Q_{3_{\delta_1}}}$	$C_{Q_{3_{\delta_2}}}$
-0.3220	0.1740	0.2326	-0.0466	-0.1903	-0.0990	0.1136	-0.0427
$C_{Q_{3_{\delta_3}}}$	$C_{Q_{3_{\delta_4}}}$	$C_{Q_{3_{\eta_1}}}$	$C_{Q_{3_{\eta_2}}}$	$C_{Q_{3_{\eta_3}}}$	$C_{Q_{3_{\dot\eta_1}}}$ V∞ (ft)	$C_{Q_{3_{\dot\eta_2}}}$ V∞ (ft)	$C_{Q_{3_{\dot\eta_3}}}$ V∞ (ft)
-0.2421	0.0093	-0.0337	-0.2531	-0.0855	-0.1593	0.0084	-0.6013

- Note: The aerodynamic damping coefficient for mode 2, $C_{Q_{2_{\dot\eta_2}}}$, was adjusted to raise the bending-torsion flutter speed. The discrepancy was attributed to the mode shape of the 1st symmetric torsion mode.

Table B3, Static-Elastically Adjusted Aerodynamic Coefficients

C_{L_α} /rad	C_{M_α} /rad	C_{L_q} /rad	C_{M_q} /rad	$C_{L_{\delta_1}}$ /rad	$C_{M_{\delta_1}}$ /rad
5.13	-26.58	4.821	-152.47	0.396	-0.090
$C_{L_{\delta_2}}$ /rad	$C_{M_{\delta_2}}$ /rad	$C_{L_{\delta_3}}$ /rad	$C_{M_{\delta_3}}$ /rad	$C_{L_{\delta_4}}$ /rad	$C_{M_{\delta_4}}$ /rad
0.447	-8.613	0.559	-15.12	0.588	-13.27
C_{D_α} /rad	$C_{D_{\delta_1}}$ /rad	$C_{D_{\delta_2}}$ /rad	$C_{D_{\delta_3}}$ /rad	$C_{D_{\delta_4}}$ /rad	
0.110	0.0010	0.0013	0.0015	0.0010	

Appendix C - Updated Equations for Aeroelastic Coefficients

Integral expressions for the aeroelastic coefficients given in Table B2 in Section 11, Appendix B are listed in Eqns. 7.94 and 7.95 in Ref. 4. But those expressions were developed under the assumption that the wing's elastic axis was coincident with the airfoil's aerodynamic center. Although this assumption simplifies the resulting equations, it is frequently not valid, as in our case here. So the streamwise distance along the chord between the elastic axis and the aerodynamic center, denoted as e_W, is not zero. In this case, the relevant integral expressions analogous to Eqns. 7.94 and 7.95 in Ref. 4 are given below. All the terms in these expressions are defined in the reference, but note that the plunge and twist components of the free-vibration mode shapes are here denoted as v_Z and v_Z', respectively.

$$C_{Q_{i_\alpha}} = -\frac{2}{S_W \overline{c}_W} \int_0^{b_W/2} c_{l_\alpha}(y)\left(v_{Z_{i_W}}(y) - e_W(y)v'_{Z_{i_W}}(y)\right)c(y)\,dy$$

$$C_{Q_{i_q}} = \frac{2}{V_\infty S_W \overline{c}_W} \int_0^{b_W/2} c_{l_\alpha}(y)\left(v_{Z_{i_W}}(y) - e_W(y)v'_{Z_{i_W}}(y)\right)\left(x_{AC_W}(y) - X_{\text{Ref}}\right)c(y)\,dy$$

$$C_{Q_{i_{\delta j}}} = -\frac{2}{S_W \overline{c}_W} \int_{\eta_{i,j}}^{\eta_{o,j}} \left(c_{l_{\delta j}}(y)v_{Z_{i_W}}(y) - \left(c_{m_{\delta j}}(y)c(y) + e_W(y)c_{l_{\delta j}}(y)\right)v'_{Z_{i_W}}(y)\right)c(y)\,dy \qquad 15$$

$$C_{Q_{i_{\eta j}}} = -\frac{2}{S_W \overline{c}_W} \int_0^{b_W/2} c_{l_\alpha}(y)\left(v'_{Z_{j_W}}(y)v_{Z_{i_W}}(y) - e_W(y)v'_{Z_{j_W}}(y)v'_{Z_{i_W}}(y)\right)c(y)\,dy$$

$$C_{Q_{i_{\dot{\eta} j}}} = -\frac{2}{V_\infty S_W \overline{c}_W} \int_0^{b_W/2} c_{l_\alpha}(y)\left(v_{Z_{j_W}}(y)v_{Z_{i_W}}(y) - e_W(y)v_{Z_{j_W}}(y)v'_{Z_{i_W}}(y)\right)c(y)\,dy$$

11. References

1. Burnett, E.L., Atkinson, C., Beranek, J., Sibbitt, B., Holm-Hansen, B., and Nicolai, L., " NDOF Simulation Model for Flight Control Development with Flight Test Correlation," Lockheed Martin Aeronautics Co., AIAA Paper No. 2010-7780, Toronto, August 2010.
2. ZAERO Theoretical Manual, ZONA Technology Inc., ZONA 02 -12.4, Scottsdale, AZ, 2011.
3. Lind, R. and Brenner, M., *Robust Aeroservoelsticity Analysis – Flight Test Application,* Springer-Verlag, New York, 1999, pp. 29-54.
4. Schmidt, David K., *Modern Flight Dynamics,* McGraw-Hill, 2012.
5. Waszak, M. and Schmidt, D.K., "Flight Dynamics of Aeroelastic Vehicles," *Journal of Aircraft,* Vol. 25, No. 6, June 1988.
6. Bisplinghoff, R. L., Ashley, H., *Principles of Aeroelasticity*. John Wiley & Sons, Inc., New York, 1962.
7. Yates, E. C., Jr., "Calculation of Flutter Characteristics for Finite-Span Swept or Unswept Wings at Subsonic and Supersonic Speeds by a Modified Strip Analysis," NACA RML57L10, 1958.

8. Kotikalpudi, A., Taylor, B., Moreno, C., Pfifer, H., and Balas, G., "Swing Tests for Estimation of Moments of Inertia," Unpublished notes, University of Minnesota Dept. of Aerospace Engineering and Mechanics, 2013.
9. USAF Stability and Control DATCOM, McDonnell Douglas Corp. for the USAF Wright Aeronautical Lab, AFWAL–TR-83-3048, April 1978.
10. USAF Stability and Control Digital DATCOM, McDonnell Douglas Corp. for the USAF Wright Aeronautical Lab, AFWAL-TR-79-3032, April, 1979.
11. Morino, C. P., "Finite-Element Structural Analysis of a Small Flexible Aircraft," Unpublished notes, University of Minnesota Dept. of Aerospace Engineering and Mechanics, 2014.
12. Moreno, C.P., Gupta, A., Pfifer, H., Taylor, B., and Balas, G., "Structural Model Identification of a Small Flexible Aircraft," Proceedings of the American Control Conference, Portland, OR, June 2014, pp. 4379-4384.
13. Gilbert, M. G., Schmidt, D.K., and Weisshaar, T. A., "Quadratic Synthesis of Integrated Active Controls for an Aeroelastic Forward-Swept-Wing Aircraft," *Journal of Guidance, Control, and Dynamics*, Vol. 7, No. 2, March-April, 1984.